ORIGINAL PAPER

Monitoring of Älvkarleby test embankment dam using 3D electrical resistivity tomography for detection of internal defects

Reyhaneh Norooz[1,2] · Aristeidis Nivorlis[1] · Per-Ivar Olsson[1,3] · Thomas Günther[4] · Christian Bernstone[5] · Torleif Dahlin[1]

Abstract

Electrical resistivity tomography (ERT) is a potential-based method for detecting internal erosion in the core of embankment dams using the electrodes installed outside. This study aims at evaluating the practical capability of ERT monitoring for detecting internal defects in embankment dams. A test embankment dam with in-built well-defined defects was built in Älvkarleby, Sweden, to assess different monitoring systems including ERT and the defect locations were unknown to the monitoring teams. Between 7500 and 14,000 ERT data points were acquired daily, which were used to create the distribution of electrical resistivity models of the dam using 3D time-lapse inversion. The inversion models revealed a layered resistivity structure in the core that might be related to variations in water content or unintentional variations in material properties. Several anomalous zones that were not associated with the defects were detected, which might be caused by unintentional variations in material properties, temperature, water content, or other installations. The results located two out of five defects in the core, horizontal and vertical crushed rock zones, with a slight location shift for the horizontal zone. The concrete block defect in the core was indicated, although not as distinctly and with a lateral shift. The two remaining defects in the core, a crushed rock zone at the abutment and a wooden block and a crushed rock zone in the filter, were not discovered. The results cannot be used to fully evaluate the capability of ERT in detecting internal erosion under typical Swedish conditions due to limited seepage associated with the defects. Furthermore, scale effects need to be considered for larger dams.

Keywords Electrical resistivity tomography · Monitoring · Embankment dam · Internal erosion · 3D inversion model

1 Introduction

As there is limited scope for the construction of new hydropower dams in many countries, the role of hydropower in a completely renewable energy system is based on the continued use of existing facilities. Hydropower embankment dams must therefore work with as close to 100% availability as possible. One major risk threatening embankment dam integrity is internal erosion of the core. Internal erosion can

✉ Reyhaneh Norooz
reyhaneh.norooz@tg.lth.se

1 Engineering Geology, Lund University, Lund, Sweden

2 AFRY AB, Malmö, Sweden

3 WSP Sverige AB, Malmö, Sweden

4 Leibniz Institute for Applied Geophysics, Hannover, Germany

5 Vattenfall AB, Solna, Sweden

under certain conditions progress inside the dam structure, but is difficult to detect early with conventional methods. If extensive internal erosion is occurring, it will be detected by downstream leakage measurements, or eventually from the creation of sinkholes. Therefore, to detect internal erosion, it is required to develop instrumentation techniques that have the capability to enhance the capability to early discover weak zones as part of the efforts to continuously improve the safety of earth embankment dams.

Electrical resistivity tomography (ERT) is a geophysical method that can measure spatial and temporal variations in the electrical resistivity (e.g., [1] and references therein). In embankment dams, internal erosion causes changes in grain size distribution and thereby resistivity and leads to anomalous seepage which induces larger variation in temperature and thereby resistivity. The temporal resistivity variation patterns caused by anomalous leakage will differ from expected resistivity variations caused by differential wetting and seasonal temperature, hence monitoring has the

potential to resolve ambiguities inherent in single time survey results. Two-dimensional (2D) ERT measurements are regularly performed in embankment dams, since 2D measurements are cost and time effective and with easy deployment of the electrodes that are needed for the survey. Surface or buried electrodes can be used for the dam surveys and the buried electrodes can increase the data resolution. In existing dams, stainless steel plate electrodes can be buried for example along the crest and the downstream toe by digging shallow pits, e.g., 1 m deep, and placing some fine-grained soil around them to reduce the electrode contact resistance [2]. Furthermore, electrode layouts can be placed on the upstream slope of the dam by divers, in a dam with relatively constant water level [2]. Electrodes can also be installed in the upper part of the dam core in connection with heightening of existing dams with the aim of increasing storage capacity [3]. Another possibility for existing dams might be to install electrodes in the dam filters via boreholes to enhance the data resolution in the core at depth. In new dams, electrodes can be installed inside the dam during the construction period.

Many researchers applied the 2D ERT method in seepage detection such as Sjödahl et al. [4]. They used short-term 2D ERT monitoring in the Røssvatn test embankment dam in Norway. The results showed that time-lapse ERT measurements in connection with changes in the reservoir level are useful for discovering leakage paths, which was confirmed by short-term monitoring on a small embankment dam conducted by Sjödahl et al. [5]. Martínez-Moreno et al. [6] used ERT and Induced polarization (IP) techniques to identify leakage and potential areas for internal erosion in the Negratín dam in Spain. The results showed the seepage zones with low resistivity and high chargeability. Masi et al. [7] designed a test rig to perform electrical resistivity measurements on a soil mixture undergoing internal erosion. The results showed that the ERT method has the potential to discover the erosion process. Shin et al. [8] used ERT to detect piping in an earthen dam model of a sandbox. This study showed that the time-lapse ERT and resistivity changes could reflect the water content variations in the dam. Lee et al. [9] used a modified resistivity array to detect leakage paths in an embankment dam in Korea. Analysis of the modified survey data indicated two zones suspected of leakage in the downstream slope. Hojat et al. [10] used ERT and fibre-optic techniques to detect seepage zones in a test embankment. The results showed that ERT measurements could discover seepage and fibre-optic sensors showed the seepage with a short delay compared to ERT. Guo et al. [11] used self-potential (SP) and ERT to discover seepage paths in an earth-filled dam which already has some signs of erosion. Three seepage paths based on the negative anomaly of SP and the low resistivity of ERT consistent with the six seepage outfalls were detected.

In embankment dams, effects from the disregarded (third) dimension effects caused by the slopes and internal material regions with different resistivity distort the ERT data, and the assumptions of infinitely extended structures perpendicular to the electrode layout in the calculation of geometric factors are no longer accurate. Thus, it is necessary to consider the distortions and the induced errors in inverse modelling. Hence, researchers used different techniques such as 3D calculations of the geometric factors and 3D inversion models to consider the distortions due to 3D effects. Cho et al. [12] studied 3D effects caused by the dam geometry and water elevation changes on ERT data collected from embankment dams and showed that the 3D effects are essential to consider in the inversion calculations. Fargier et al. [13] presented a new approach for calculating apparent resistivity values from the measured data collected from an embankment dike based on redefining the normalization principle. The results showed that apparent resistivity values that are compensated for the external 3D effects yield more reliable results when processed within a 2D conventional inversion scheme. Bièvre et al. [14] used 3D computation of geometric factors in a 2D inversion model and could improve the interpretation of 2D ERT data collected from a dyke. These techniques for compensation for the 3D character of the surface geometry, would however not work for handling the 3D effects caused by the internal zonation of typical Swedish embankment dams. Norooz et al. [15] developed a 3D ERT inverse model as a pre-study for ERT measurements in Älvkarleby test embankment dam in Sweden. They used priori information about the resistivity of different zones of the test dam in the inversion model. The proposed methodology could decrease non-uniqueness in the inversion and make time-lapse ERT a useful monitoring tool. The mentioned 3D effects on ERT data need to be further studied and a methodology with an inverse model considering the 3D context of embankment dams is required.

The purpose of this study is to assess the capability of ERT measurements as a monitoring tool for internal erosion detection in embankment dams applying inverse modelling considering the 3D character of embankment dams. A test embankment dam with a height of 4 m, containing some intentional artificial defects in the core and fine filter, was constructed in Älvkarleby with the purpose of assessing different monitoring techniques including ERT. This study was carried out within that framework, whereas the 3D geometry of the dam, the internal zonation and the 3D calculation of the geometric factor were incorporated in the inversion modelling.

2 Materials and methods

2.1 Älvkarleby test embankment dam

Vattenfall R&D has built a test embankment dam (Fig. 1) at their laboratories in Älvkarleby, Eastern Sweden [16]. The dam stands in a concrete container with an inner dimension of 20 m length × 16 m width × 4 m height. It is designed as a small-scale version of a typical Swedish embankment dam, with internal zonation consisting of a dam core made from hydraulically tight fine-grained till, fine filters and coarse filters on either side of the core, and structural fill (see Table 1 and Fig. 2a). Defects were integrated in the embankment dam with the purpose of evaluating the detection capability of different methods, where ERT was one of the methods. The test was designed as a blind test, with a team at Vattenfall who designed the defects and the locations of these were kept secret to the investigation teams.

Several artificially made small defects were placed inside the core and fine filter (the red rectangles in Fig. 2b, c), and different monitoring instruments including ERT were used in an attempt to evaluate their capability to locate the defects. The shape, size and defects' positions are shown in Table 2. The defects include a wooden block intended to simulate a cavity (Defect No. 1 in Figs. 2b, c, 3a), two horizontal permeable zones (Defects No. 2 and 5 in Figs. 2b, c, 3b), one vertical loose zone (Defect No. 3 in Figs. 2b, c, 3c) and one lump of concrete intended to simulate a block of stone (Defect No. 4 in Figs. 2b, c, 3d). One filter defect was also placed in the fine filter (Defect No. 6 in Figs. 2b, c, 3e). Defects No. 2, 3 and 5 are specifically designed to simulate internal erosion, but other defects were places in the dam body to have inhomogeneity in the dam material and assess the ability of different monitoring methods in detecting both anomalies in the material properties and zones affected by the internal erosion.

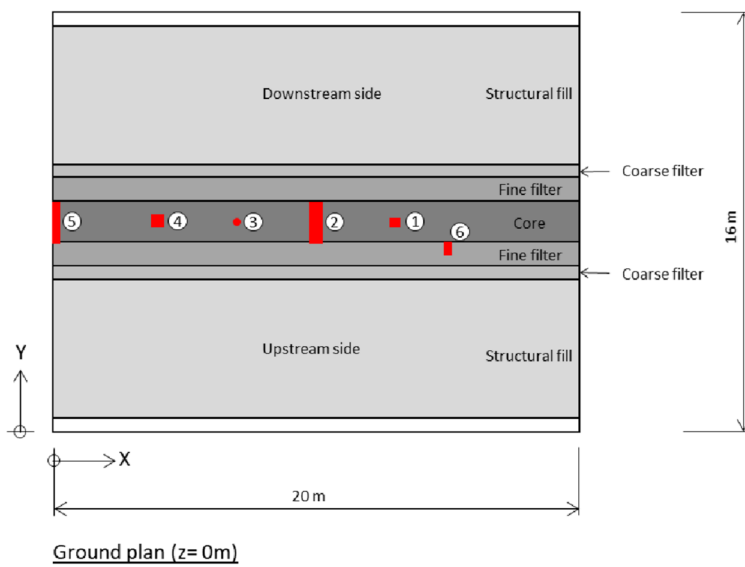**Fig. 1** Aerial view of Älvkarleby test dam [16]

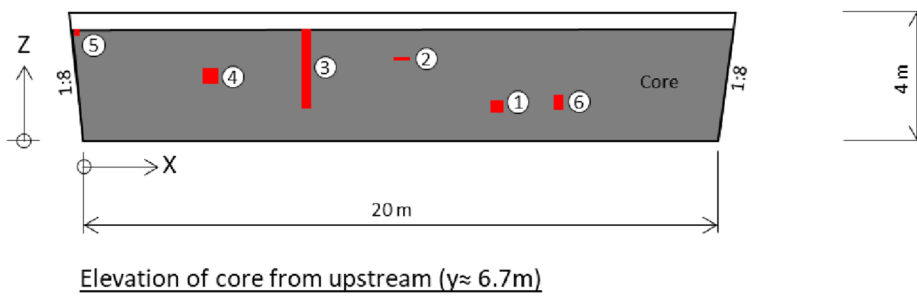**Table 1** Material properties according to preliminary testing [16]

|	Core	Fine filter	Coarse filter	Structural fill
Material	Moraine (0–20 mm)	Crushed rock (0–16 mm)	Crushed rock (8–64 mm)	Crushed rock (32–154 mm)
Hydraulic conductivity	10^{-7} m/s	10^{-5} m/s	10^{-2} m/s	10^{-1} m/s
Density	2.25 t/m³	1.9 t/m³	1.7 t/m³	1.8 t/m³
Friction angle	42˚	36˚	40˚	41˚
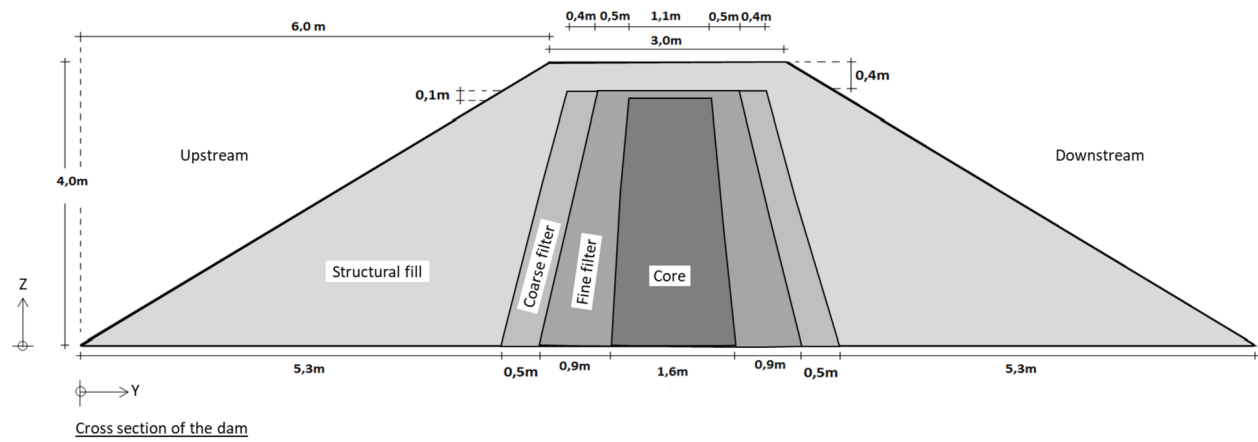
Fig. 2 **a** Cross section of Älvkarleby test dam. **b** Ground plan of the dam with defects in red. **c** Cross section of the core from upstream ($y \approx 6.7$ m) with defects in red [17] (color figure online)

Table 2 Defects placed in the core and fine filter [17]

No.	Type	Material	Shape	Size (m)	Position			Comment
					X	Y	Z	
1	Cavity	Wood	Cube	0.4×0.4×0.4	13.0	7.5	1.0	Centrally in the core
2	Horizontal permeable zone centrally	Crushed rock, 4–8 mm	Cuboid	0.5×0.1	10.0	7.5	2.5	Through the core
3	Vertical loose zone	Crushed rock, 8–64 mm	Cylinder	0.3	7.0	7.5	3.5	Coordinates for the top
					7.0	7.5	1.0	Coordinates for the bottom
4	Boulder	Concrete cube	Cube	0.5×0.5×0.5	4.0	7.5	2.0	Centrally in the core
5	Horizontal permeable zone—at the abutment	Crushed rock, 4–8 mm	Cuboid	0.2×0.2	0.0	7.5	3.0	Through the core
6	Fine filter defect on the upstream side	Crushed rock, 8–64 mm	Cuboid	0.3×0.3	15.0	6.6	1.5	Coordinates for the top
					15.0	6.6	1.0	Coordinates for the bottom

a

b

c

d

e
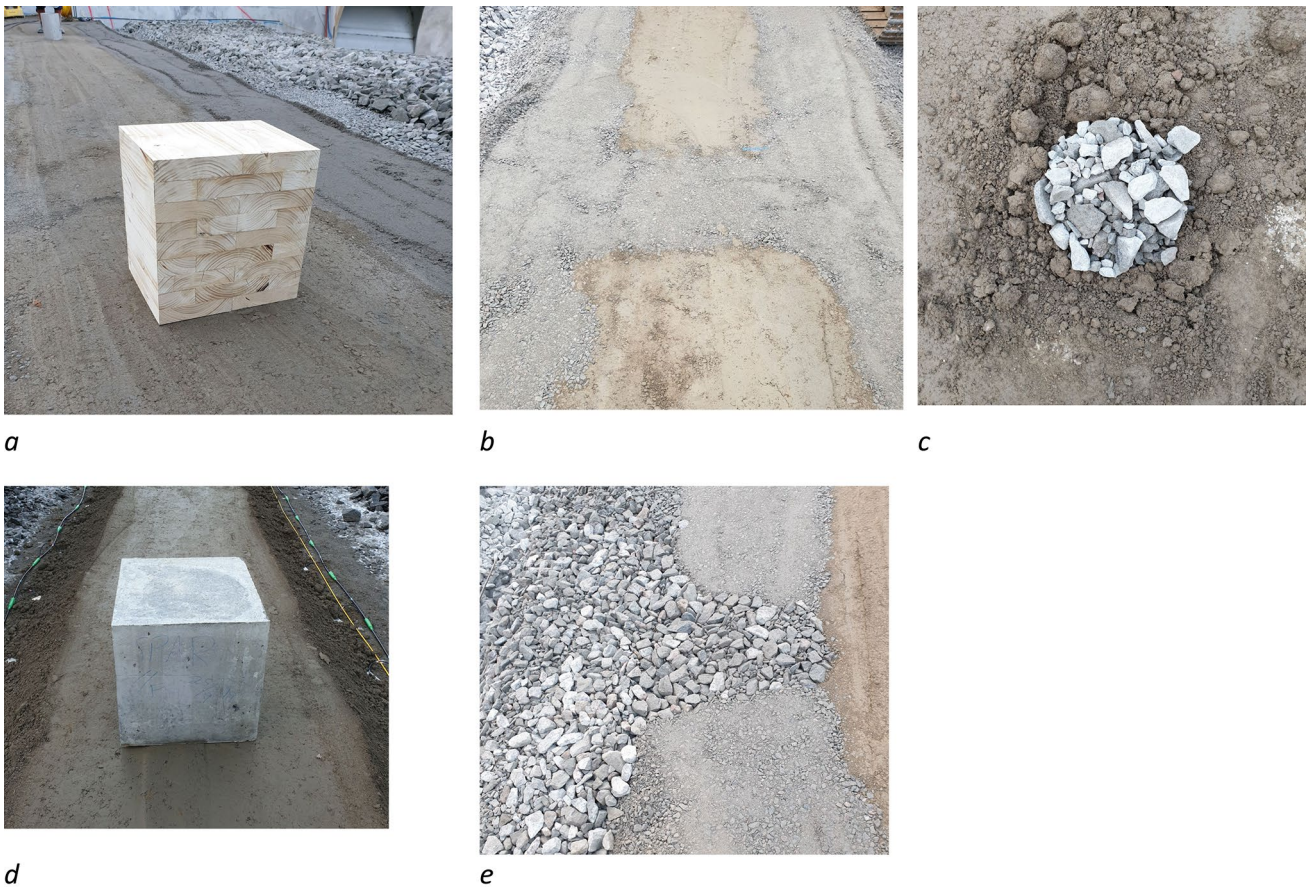
Fig. 3 The defects incorporated inside the core and filter. **a** The cavity in the core (Defect No. 1). **b** The horizontal permeable zones in the core (Defects No. 2 and 5). **c** The vertical loose zone in the core (Defect No. 3). **d** The lump of concrete in the core (Defect No. 4). **e** The filter defect (Defect No. 6) [17]

2.2 ERT monitoring system

In total, 224 electrodes were installed in the test embankment for ERT. Figure 4 shows the 3D placement of the electrode spreads. The electrodes consist of 80 mm × 80 mm stainless steel plates [18], made from 0.5 mm acid-grade stainless steel. In Fig. 5, the stainless steel plates used in the measurement lines on top of the core with the seismic cables and plastic pipes which contain other installations are shown. According to the modelling in [18], the plate dimensions are small enough so that they can be considered
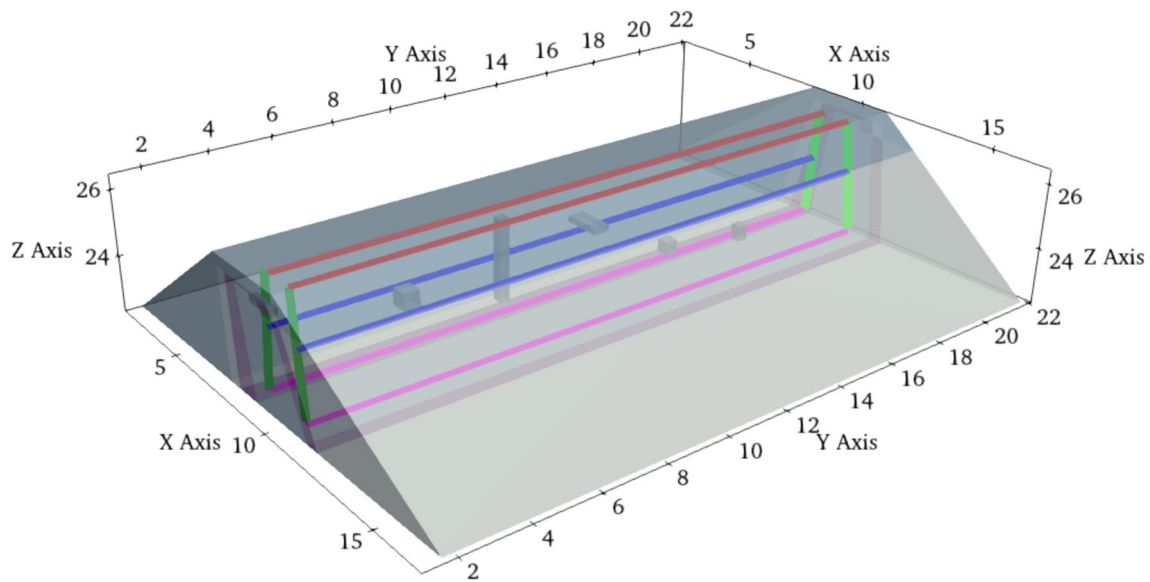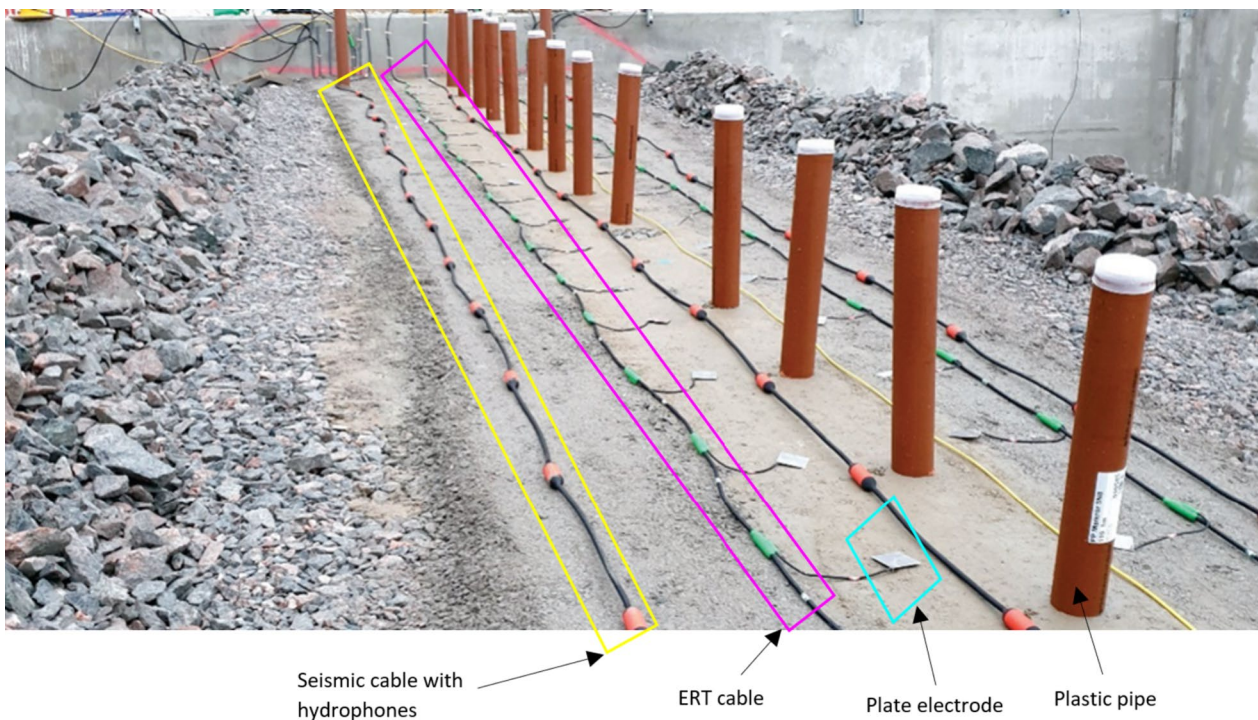
Fig. 4 Position of measurement lines

Fig. 5 Sensor installations along the top of the crest of the dam core, where the acid-grade stainless steel plates are used as ERT electrodes. The plastic pipes are intended for the seismic source [16]

points (within less than 1% modelling error) in the subsequent analysis.

The electrode installations were designed to give as good resolution as possible of the core, with a reasonable number of electrodes. No electrodes were placed in the core itself because it was not considered as a realistic option for installations in existing dams. Six horizontal electrode lines using 32 electrodes each with 61–63 cm (planned) spacing were buried: on top of the clay core and at two levels in the filters adjacent to the core, bottom, and middle. In addition, four (near) vertical electrode lines with eight electrodes each with 50 cm vertical spacing were installed at each

end in the filter of the dam. The ERT team was not on site during the construction of the dam and installation of the electrodes, but the recorded positions of the electrodes revealed that they had been placed very irregularly instead of with constant separations within each layout line as was intended. This had consequences for the finite element mesh generation as described below.

A permanently installed data acquisition system measures a full set of data and sends it to a server automatically every day. The system consists of an ABEM Terrameter LS2, a tailor-made relay switch with built-in lightning protection, an industry PC and a network router (Fig. 6). The relay switch makes it possible to select which 2×32 electrodes out of 8×32 electrodes to connect to the instrument. The monitoring sequence and data transfer are controlled by the PC via Python scripts.

Several types of configurations including bipole–bipole [19], extended gradient [20], multiple gradient [21] and corner [22] arrays were used in the ERT measurements. The measurement sequences were designed in a way to provide enough data points that can cover the whole core volume and increase the defect detection capability for defects in it. To improve core data coverage, the profiles were placed in the direct vicinity of the core and not along the surface, as that would have resulted in poorer coverage of the deeper parts of the core and stronger weather dependence. The crossline measurements between horizontal profiles at different elevations could cover the middle area of the core. The crossline measurements between the inclined profiles near the right and left abutments were intended to provide enough data at the ends to discover defects near the abutments. The

corner arrays between the inclined and horizontal lines could cover the areas near the upstream and downstream borders of the core and the fine filter. Furthermore, an extended gradient array applied in each horizontal line supported other collected data points in addition to obtaining data near the upstream and downstream core borders with the filter. Initially, around 7500 ERT data points were collected daily, which was increased in a couple of steps to be around 14,000 in the later part of the monitoring by adding non-standard and asymmetric electrode combinations. Hence, the size of the data sets used in the inverse modelling has increased accordingly.

The contact resistance of the electrodes, which was measured with the focus-one technique [23], falls between some hundred and a few thousand Ω. A statistical summary including mean, maximum, minimum and standard deviation of the contact resistance for each layout for the entire monitoring period is summarized in Table 3. It shows that the contact resistance for all the layouts is moderate and in an acceptable range.

2.3 Reciprocal data error analysis

Assuming a single resistivity measurement which uses four electrodes, A and B are for current injection, and M and N for measuring potential. The reciprocal of that measurement would then use M and N for the current injection and A and B for potential. The reciprocity theorem states that by reversing the current and potential dipoles, the measurement should be the same; therefore, any differences on the two measurements should be attributed to error and/or noise. Reciprocal analysis can be used for assessing the error in resistivity surveys [24]; however, it comes with the cost of increasing the acquisition time. Especially for nested arrays, which have a better signal-to-noise ratio, the increase in acquisition time is significant and the reciprocal data tends to be noisier due to the longer M to N separations. In the work presented in this paper, most of the data were collected using nested arrays (extended multiple
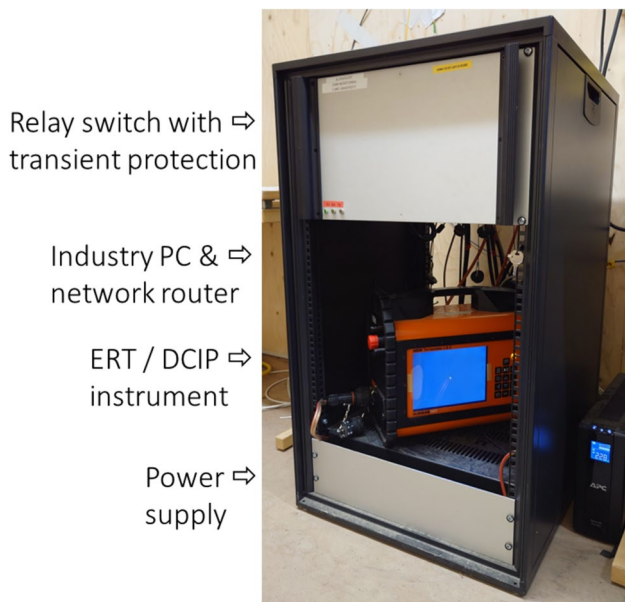

Fig. 6 ERT acquisition system at the Älvkarleby test dam

Table 3 Statistical summary of the contact resistance for each layout for the entire monitoring period

Layout	Mean R_c [Ω]	Min R_c [Ω]	Max R_c [Ω]	Std. dev.
Crest upstream	1022	727	1442	121
Crest downstream	1840	1078	3056	273
Mid upstream	1456	671	2480	255
Mid downstream	1615	933	2473	224
Bottom upstream	1333	764	1824	179
Bottom downstream	1861	567	2672	525
Ends layout	2492	1611	3467	350
Total	1659	567	3467	528

Table 4 The collected reciprocal data

Task	Layout	# of reciprocals
1	Crest upstream–crest downstream	118
2	Mid upstream–mid downstream	118
3	Bottom upstream–bottom downstream	118
4	Crest upstream–bottom downstream	118
5	Crest downstream–bottom upstream	118
6	End layouts	44
7	Crest upstream–mid upstream	118
8	Mid upstream–bottom upstream	118
9	Crest downstream–mid downstream	118
10	Mid downstream–bottom downstream	118
Total		1106

gradient); however, a number of crossline bipole measurements were included and used to quantify the reciprocal error. A total of 1106 (around 10% of the total daily data acquired) reciprocal measurements were collected throughout all the layouts (Table 4).

The quality of the measurements was assessed by analysing the reciprocal error. The reciprocal error was calculated as a percentage difference between the two resistivity measurements using the formula:

$$R_{error} = \frac{|R_1 - R_2|}{\left|\frac{R_1 + R_2}{2}\right|} \times 100\%, \tag{1}$$

where R_{error} is the reciprocal error in percent. R_1 is the measured resistivity when electrodes A and B are the current electrodes, and electrodes M and N are the potential electrodes. R_2 is the measured resistivity when electrodes M and N are the current electrodes and electrodes A and B are the potential electrodes. Due to the limited number of reciprocals, the data were not analysed in a statistical way depending on the measured resistance like [24], but in the dependency of the contact resistance.

The reciprocal error against contact resistance for the data points with the reciprocal data collected 2020-10-06 is presented in Fig. 7 as an example result from a single day. The average reciprocal errors for the data points with reciprocal data collected each day for each task are presented in Fig. 8. The reciprocal error was generally below 1% for all tasks and seems to be unrelated to high contact resistances, which are not exceedingly high. There are very few individual outliers with higher reciprocal error, most of which are related to the crest layouts (Fig. 8). The average reciprocal error is below 1% for the entire period for all tasks, except Task 1 (crest layout) and Task 6 (end layout). For Task 1 the reciprocal is generally noisy, especially during the summer periods which could be attributed to low moisture content. The reciprocal error is, however, not higher when any of the crest layouts are used in combination with another layout (Tasks 4, 5, 7, 9), but only when measuring between the two crest layouts. For Task 6, the reciprocal is generally stable, but higher than those of the other tasks (still below 5% over the entire period).
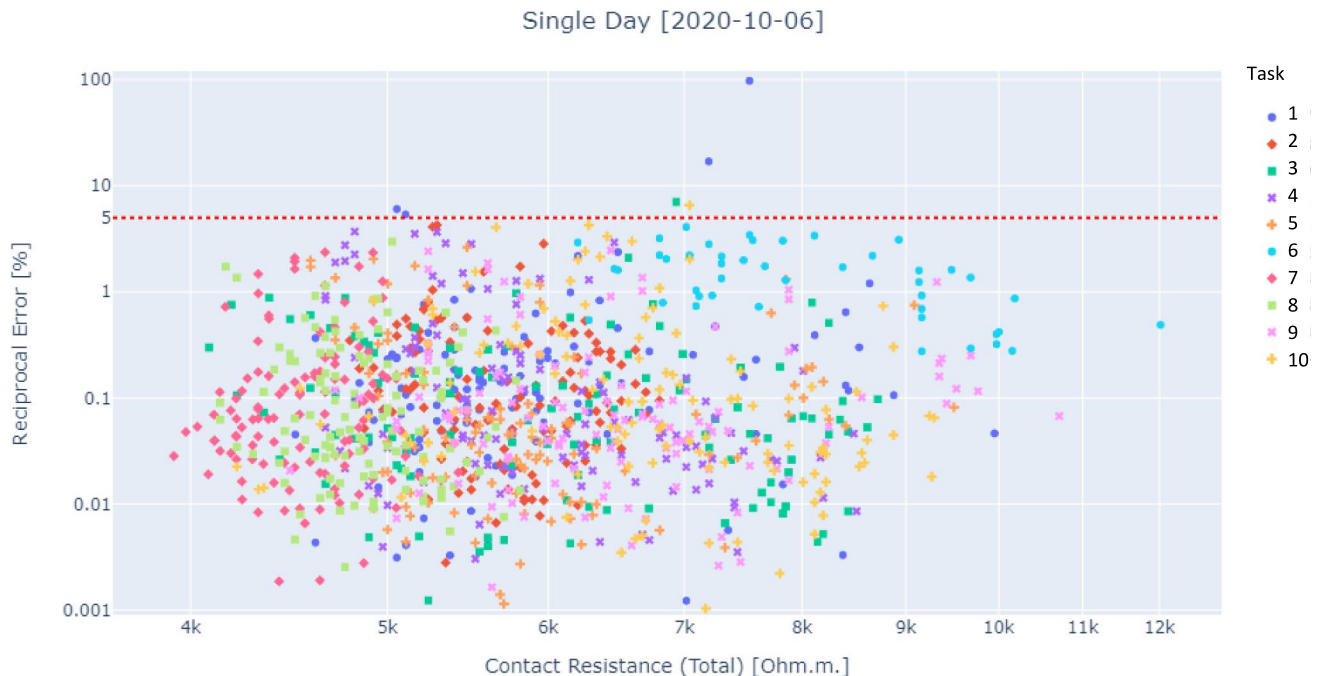
Fig. 7 The reciprocal error against contacts' resistance for whole data points collected in 2020-10-06
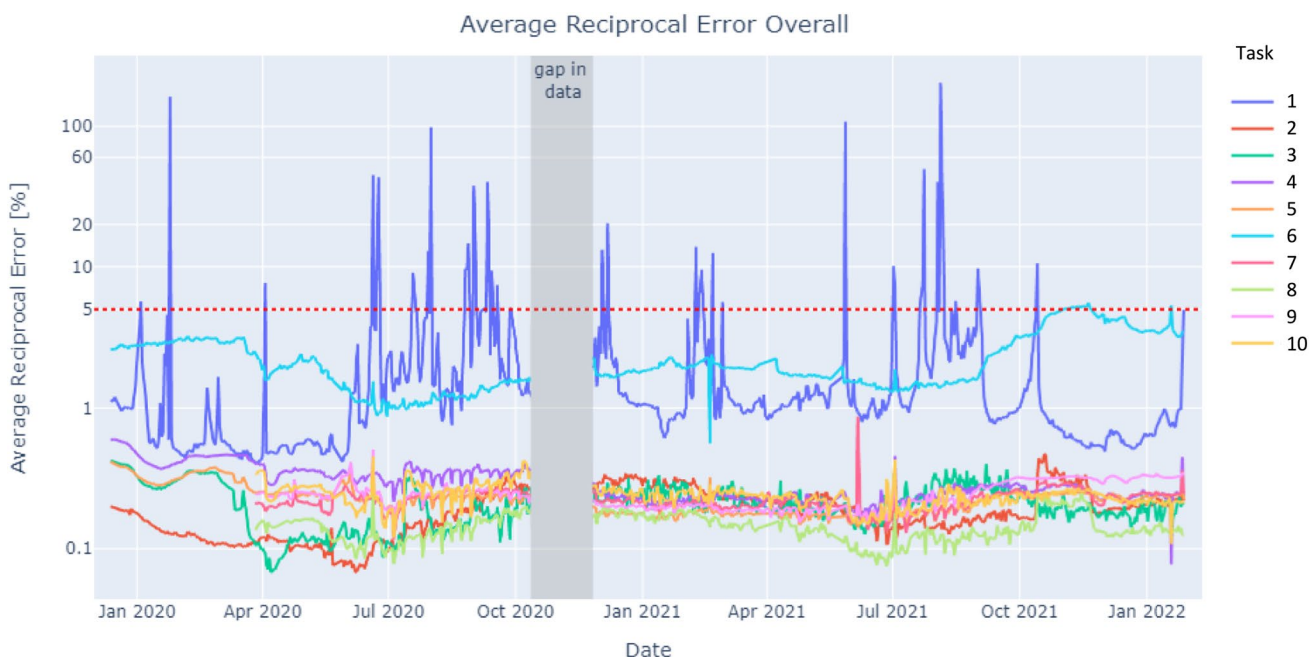
Fig. 8 Average reciprocal error for whole data points collected each day for each task

The analysis of the reciprocal error shows that the data quality is mostly exceptionally high, with < 1% error for most layouts; however, the measurements coming from the two crest layouts are prone to have larger errors. There does not seem to be any obvious relation between the higher reciprocal error levels for the crest layout and contact resistance (Table 3), which could otherwise have been a possible explanation.

2.4 Inverse numerical modelling

In the electrical resistivity measurements, the apparent resistivity is defined as follows:

$$\rho_{\text{apparent}} = K \cdot R = \frac{K \cdot V_{MN}}{I}, \tag{2}$$

where ρ_{apparent} is the apparent resistivity in Ωm, K is the geometric factor in m, R is the electrical resistance in Ω and V_{MN} is the measured electrical potential difference between potential electrodes M and N in volts. I is the current injected through the current electrodes, A and B in amperes.

The analytical geometric factor for a four-electrode measurement is calculated as follows:

$$K_{\text{analytical}} = 2\pi \left(\frac{1}{AM} - \frac{1}{BM} - \frac{1}{AN} + \frac{1}{BN} \right)^{-1}, \tag{3}$$

where AM, AN, BM and BN are the respective distances between electrodes in m. This factor is related to the array type and is accurate for an infinite flat subsurface.

Inverse numerical modelling (inversion) was used to recover the resistivity distribution in the dam, in which a finite element method (FEM) model of the resistivity distribution in the dam is adjusted in an iterative process that seeks to minimize the difference between the calculated model response and measured apparent resistivities (residuals). Although the primary interest is the properties of the dam core, it is necessary to include all parts of the dam as well as the concrete container and surrounding ground to be able to recover the resistivity distribution in the core without distortions that would otherwise affect it. The measured data sets are, however, as mentioned before, optimized for resolution of the resistivity distribution of the core.

An L1 norm reweighting scheme was used for the inversion to enforce the model gradients [25, 26]:

$$\left(J_k^T R_d^T R_d J_k + \lambda F \right) \Delta q_k = J_k^T R_d g - \lambda F q_k, \tag{4}$$

$$g = y - f, \tag{5}$$

in which J_k is the Jacobian matrix, and λ is the damping factor. F is the smoothing matrix, Δq_k is the model parameter change vector in the kth iteration, R_d is the weighting matrix giving equal weight to the data misfit vector, g is the data misfit vector, q_k is the model parameter in the kth iteration, y is the apparent resistivity and f is the model response which is calculated using the governing equation of the geo-electrical modelling:

$$-\nabla\left[\sigma(x,y,z)V(x,y,z)\right] + \nabla J_s(x,y,z) = 0, \qquad (6)$$

in which σ is the electrical conductivity, V is the electrical potential and j_s is the current density.

The Python-based software package pyBERT (Python Boundless Electrical Resistivity Tomography)/pyGIMLi (Python Geophysical Inverse Modelling Library) [27] was used for the inversion of the ERT data as well as for forward modelling. In this research, 3D time-lapse inversion model with 3D geometric factor calculations was used. Around 200,000 cells were generated for the inversion model using the TetGen software [28] (Fig. 9).

To avoid smooth transitions and consider the sharp transitions between the dam zones, robust ($L1$) methods were applied. A Lambda value of 40 was used. The noise was assumed to be 1% plus a voltage resolution of 25 mV. In the time-lapse model, a reference model-based scheme which applies a full minimization in each frame was used, where the model differences to the first frame are constrained. 12 regions were simulated in the geometry of the model which are shown in Table 5 and Fig. 10. In the study by Norooz et al. [15], prior information concerning the known distribution of materials in the embankment was applied in the inversion model containing the synthetic ERT data. Different region control files (settings for the constraints inside of the individual regions) with various boundaries were used in the inversion, which was however not used for the inversion here where only decoupling between the dam regions was used.

**Table 5** Simulated regions in the inversion model

Material marker	Region
1	Outer space
2	Reservoir
3	Support material (wet)
4	Support material (dry)
5	Upstream coarse filter (wet)
6	Downstream coarse filter (dry)
7	Fine filter (wet)
8	Fine filter (dry)
9	Downstream coarse filter (dry)
10	Core
11	Concrete
12	Outer box

3 Results and discussion

3.1 Synthetic models

Three synthetic data sets using pyBERT/pyGIMLi were generated, one without defects and two with five small defects in the core. The material resistivity values used in the forward modelling, which are presented in Table 6, are based on the laboratory measurements in combination with literature references [2, 29–31].

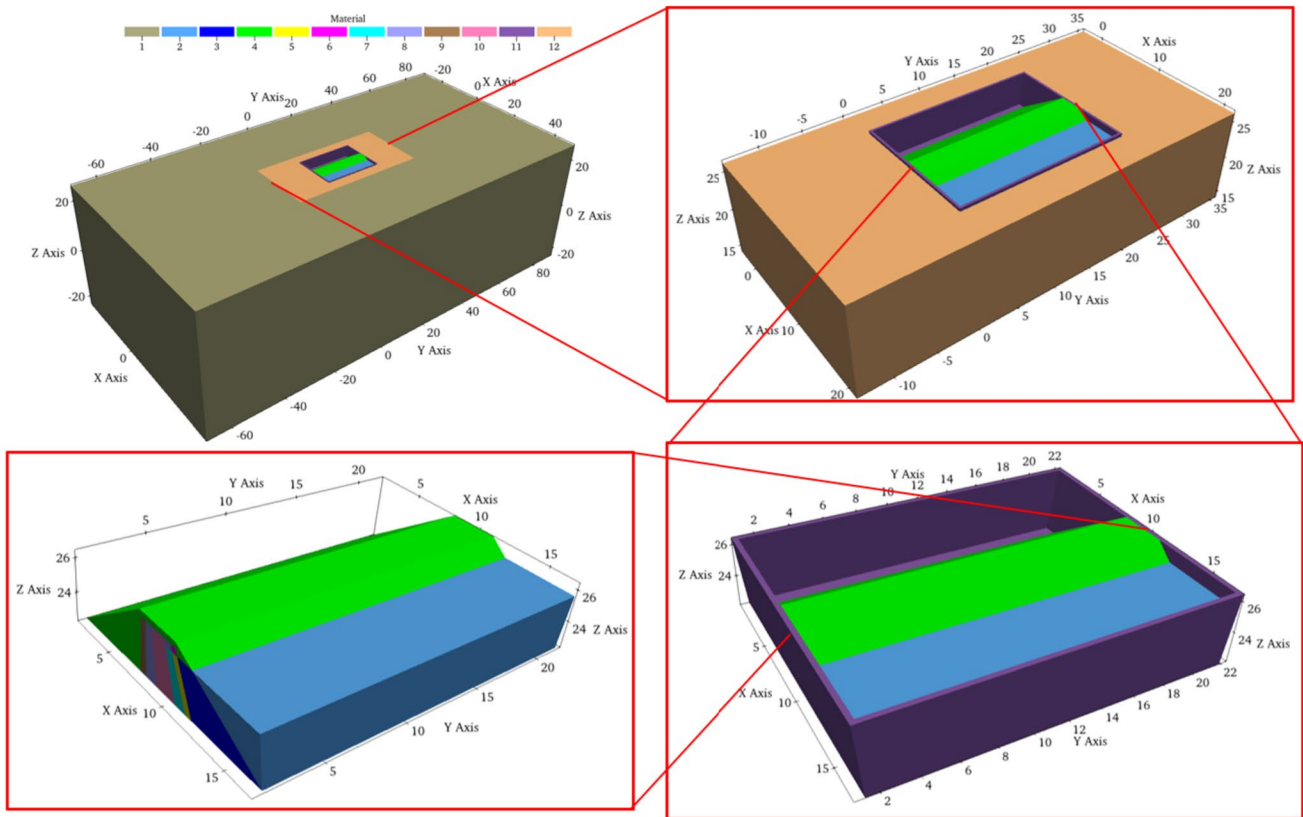**Fig. 9** The generated mesh for the inversion model
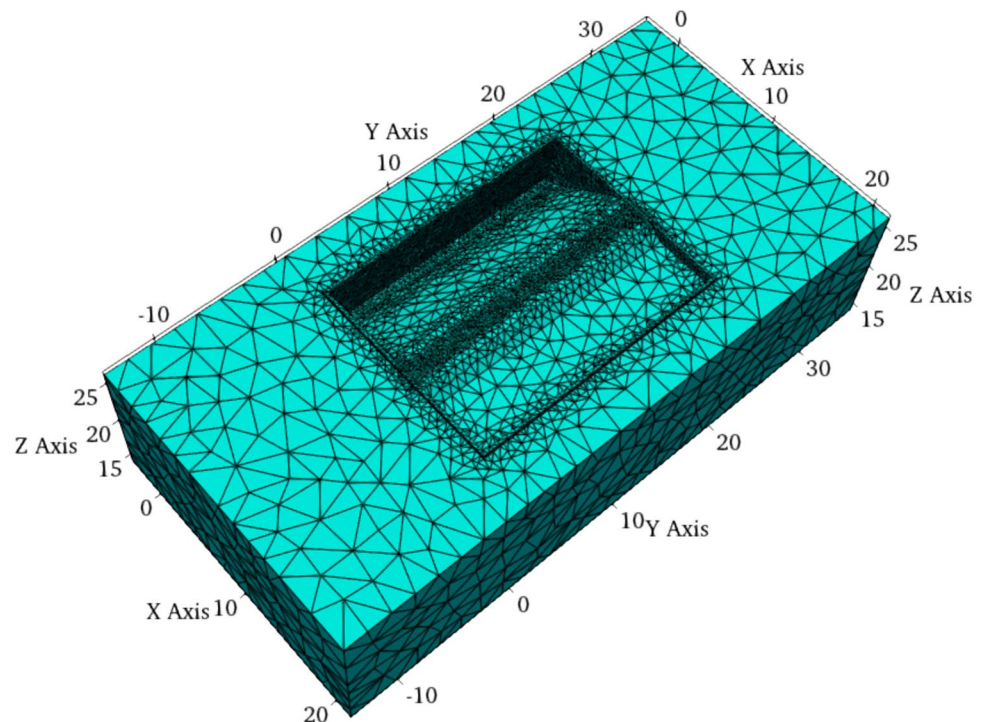
Fig. 10 Inversion model geometry separated into distinct regions

Table 6 Material resistivity used in the forward modelling

Material marker	Region	Resistivity (Ωm)
1	Outer space	300
2	Reservoir	250
3	Support material (wet)	1500
4	Support material (dry)	2500
5	Upstream coarse filter (wet)	500
6	Downstream coarse filter (dry)	2000
7	Fine filter (wet)	200
8	Fine filter (dry)	1000
9	Downstream coarse filter (dry)	2000
10	Core	50
11	Concrete	300
12	Outer box	300
13	Cavity (Defect No. 1)	5000
14	Horizontal permeable zone centrally (Defect No. 2)	500
15	Vertical loose zone (Defect No. 3)	500
16	Boulder (Defect No. 4)	5000
17	Horizontal permeable zone—at the abutment (Defect No. 5)	500

The modelled defects are based on the actual defects in the core after they had been revealed to the ERT team. Defect No. 2 (see Table 7) in the first synthetic model is larger in the model than in reality since the TetGen mesh generator was not able to generate meshes with smaller defects, the rest of the defects have the same size as the real defects. In the second synthetic model, defects No. 1, 2, 3 and 5 have a larger size than the real defects (see Table 7) to be able to compare the results of the model containing larger defects with the model containing smaller defects.

As mentioned before, in both synthetic models, one synthetic data set without defects was also generated. The data sets with the defects were inverted considering the data set without defects as the reference model and with the same settings, as used in the inverse modelling of the field ERT data.

The inversion results in a cross section in the core were taken out from the models to investigate the defect positions in the core (Fig. 11).

The inversion results along a cross section in the middle of the core (Fig. 11) are shown in Fig. 12. The synthetic data set without defects produces an almost homogeneous inverted model.

The analyses of the first synthetic ERT data with defects could partly detect the location of the simulated Defects

Table 7 Defects placed in the synthetic models

No.	Shape	Real size (m)	The size used in the first synthetic model (m)	The size used in the second synthetic model (m)	Comment
1	Cube	0.4×0.4×0.4	0.4×0.4×0.4	0.5×0.5×0.5	Centrally in the core
2	Cuboid in the dam and the first synthetic model/cube in the second synthetic model	0.5×0.1	0.5×0.2	0.5×0.5	Through the core
3	Cylinder in the dam/cuboid in both synthetic models	Diameter 0.3, height 2.5	0.3×0.3×2.5	0.5×0.5×2.5	–
4	Cube	0.5×0.5×0.5	0.5×0.5×0.5	0.5×0.5×0.5	Centrally in the core
5	Cuboid	0.2×0.2	0.2×0.2	0.5×0.5	Through the core
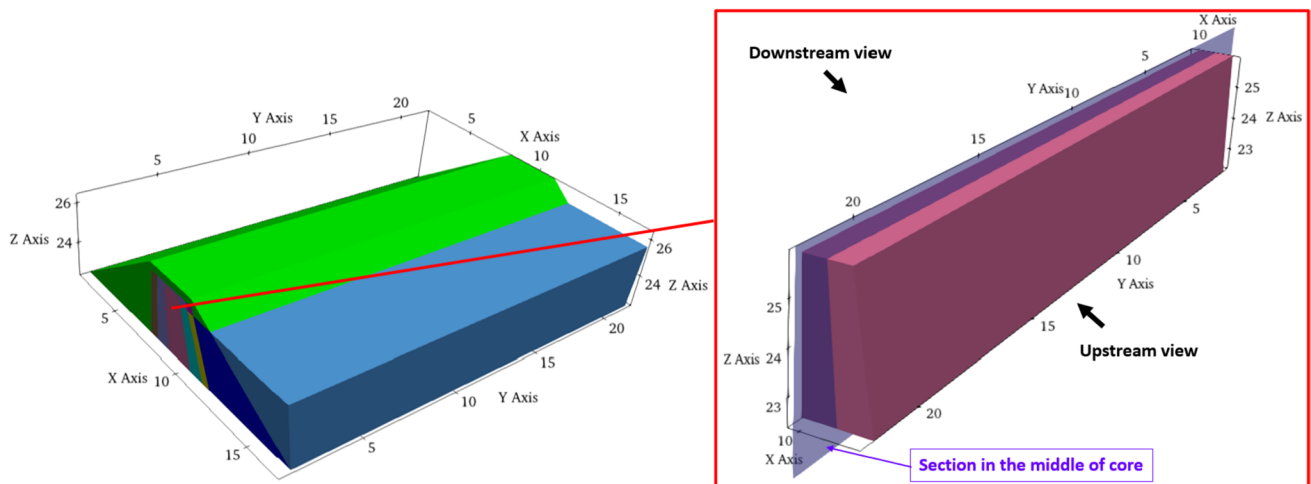
Fig. 11 The position of the cross section in the middle of the core and the upstream and downstream view of the uncovered core

No. 2, 3 and 4 with areas with higher resistivity values (Fig. 12b); however, there is a shift between the location of Defect No. 4 and the area with high resistivity.

It is difficult to interpret high-resistivity areas around Defect No. 1 as the location of this defect in the inversion results of the first synthetic model and Defect No. 5 could not be revealed by this model as well (Fig. 12b).

There are some artefacts with high resistivity in the inversion results of both synthetic models which make it difficult to interpret the location of defects.

The inversion results of the second synthetic model with defects could discover Defects No. 2 and 3 with a good resolution (Fig. 12c). Additionally, there are some high-resistivity areas around Defects No. 1, 4 and 5 in this model which shows that the second model could partly discover these three defects.

Three schemes were used for the time-lapse inversion model of field data to track the resistivity variations and examine the effects of water level changes on the results. As mentioned before the measurements have been done on a daily basis, but only the data set of one day per week was used (one every seven days) in all models. The following inversion schemes were made:

1. inverting the whole data sets (around 100 data sets) with the first data set as the reference model;
2. inverting the data sets during decreasing water levels containing around 20 data sets with the first data set as the reference model;
3. inverting the data sets during the maximum constant water level containing around 30 data sets with the last data set as the reference model.

3.2 Monitoring data

First, it should be pointed out that the value of time-lapse evaluation of the resistivity as a tool to discover the intentional defects can be expected to be limited in relation to what would be the case with ongoing internal erosion or anomalous seepage. This is caused by limited continuous throughflow of water in the anomalous zones, which is intentional because the dam design team wanted to avoid
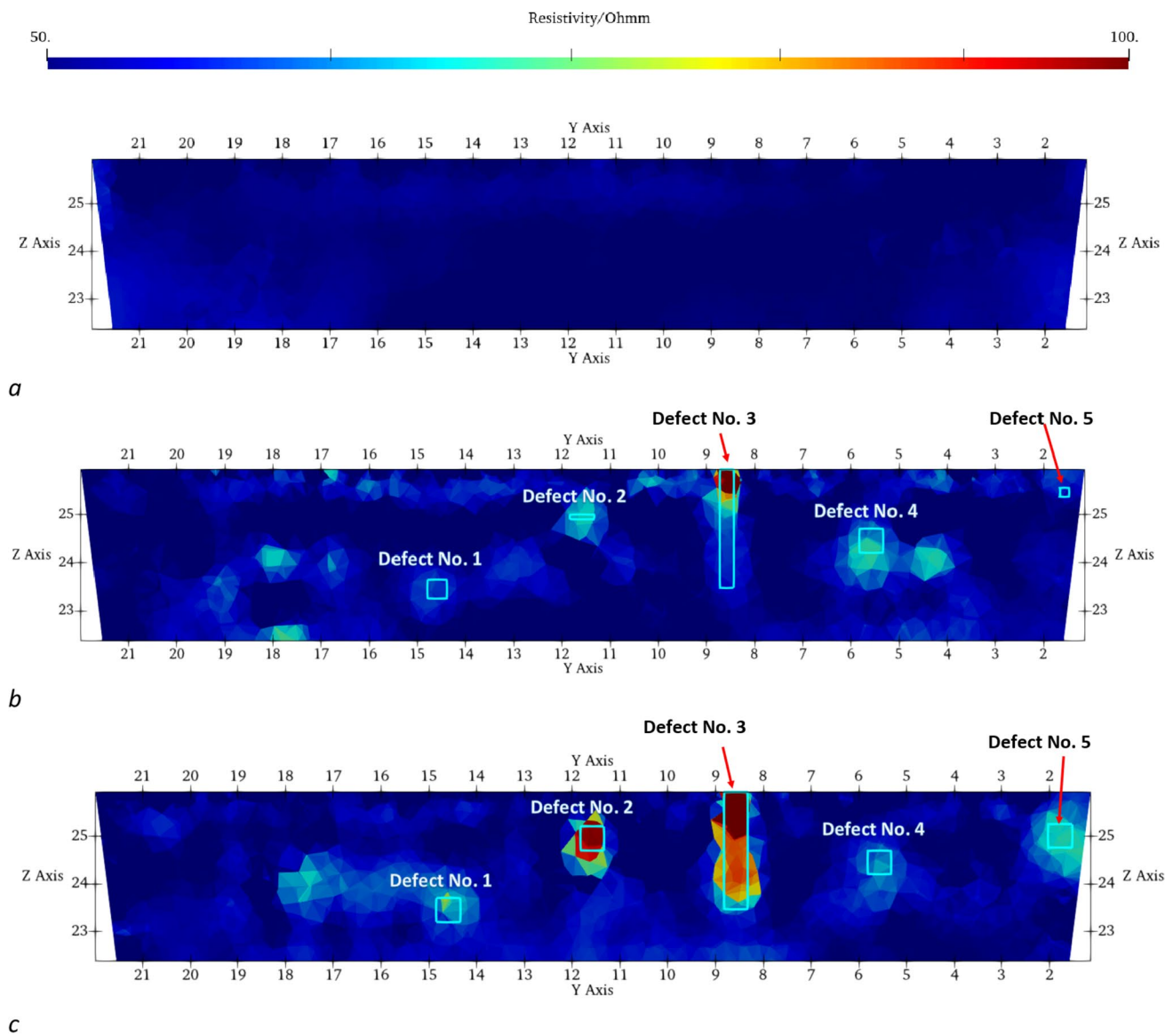
Fig. 12 The inversion results of the synthetic ERT data in the core for **a** the model without defects; **b** the first synthetic model containing defects (the location of the simulated defects is shown by blue cuboids); **c** the second synthetic model containing defects (the location of the simulated defects is shown by blue cuboids) (color figure online)

internal erosion that might lead to stability problems. The small throughflow was accomplished by fine filters on either side of the core that are hydraulically rather tight in combination with a small hydraulic gradient that follows with the shallow position of the defects (at the time of first filling the throughflow was quite high, and thereafter continuously decreasing to a low flow) [16]. The other types of simulated defects are not associated with any anomalous flow and can thus not be expected to have seasonal variations in a way that differs significantly from the rest of the dam core. Due to the lack of zones with significant anomalous throughflow, it is not possible to evaluate the capability of ERT for detecting actual zones

with internal erosion associated with the anomalous flow and coupled seasonal temperature-induced resistivity variation. On the other hand, the electrode layouts on three levels in the dam, which are advantageous for the resolution, would be challenging to install in an existing dam.

In the following, the results for the first inversion scheme are presented, and since the other scheme does not show any significant difference from the other two schemes, these results are not presented. As mentioned before, around 100 data sets (each data set in one time frame) were used in the following inversion model and the data misfit was less than 2% for each time frame which belongs to a single data set.

The inversion results of field ERT data including the data sets collected from 2019-12-12 to 2022-01-28 while the water level has been fluctuating are presented in the following. The first data set (data set 2019-12-12) was chosen as the reference model.

The following analysis focuses on the average, maximum and minimum of the inverted resistivity values that are shown in Fig. 13 for the whole period (from 2019-12-12 to 2022-01-28). A cross section in the middle of the core is visualized without the rest of the model as it is of main
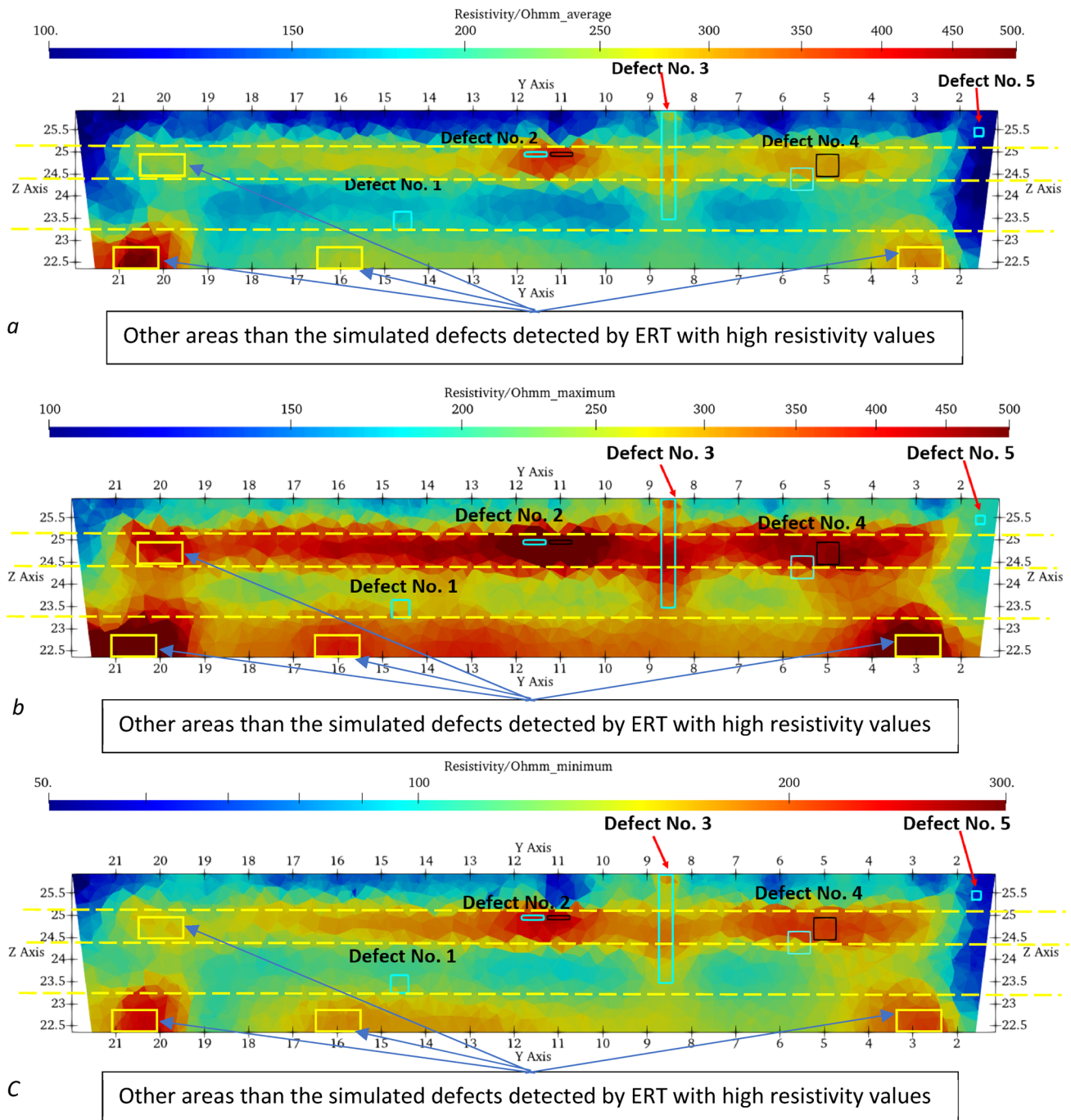
Fig. 13 The average (**a**), maximum (**b**) and minimum (**c**) values of the inverted resistivity through the whole period (from 2019–12-12 to 2022–01-28). The location of the defects is shown by blue bounding boxes, whereas the predicted location is indicated by black bounding boxes (color figure online)

interest (see the position of the cross section in the middle of the core in Fig. 11).

The models have a layered appearance, with (starting from the bottom) higher, lower, higher and lower resistivity (the dashed lines illustrate different layers in Fig. 13). This could be related to differential wetting and the geotechnical instrumentation shows that the wetting of the core happened unevenly [16]. It is likely very difficult to avoid those preferential pathways established for the water entering the core. The water will force itself to the easiest way through the core and adjacent volumes of the core will wet slowly. Among other factors that could create a layering in the resistivity are possible variations in the grading of the material, differences in compaction during construction or temperature variation. Such variation in resistivity might contain valuable information that is related to the long-term performance of the dam.

Defect No. 1 (see Table 2), a simulated cavity built from wood, was not discovered (Fig. 13a–c). In the first synthetic inversion model, Defect No. 1 which was modelled as a cube with high resistivity with the same size as the real defect was not discovered (Fig. 12b). However, in the second synthetic model, some high-resistivity areas around Defect No. 1 which were modelled with a slightly larger size than the real defect were observed (Fig. 12c). The inversion model with the field data has not indicated any high-resistivity area around (Fig. 13a–c), but in addition to the relatively small size of the defect, water absorption by the wood can have made the resistivity contrast small relative to the surrounding core material, and thus hard to detect. Water-saturated wood may have a resistivity of significantly less than 100 Ωm [32] (Fig. 13a–c).

Defect No. 2 (see Table 2), which is a horizontal permeable zone made of crushed rock, was detected. However, the model predicted the location with some distance from the real location which is indicated by the blue bounding boxes in Fig. 13a–c. The predicted location of the defect is shown by the back bounding boxes in Fig. 13a–c, where the bounding boxes are placed at the centre of the area with the high resistivity (Fig. 13a–c). This zone has a significantly higher resistivity than the surrounding clay material.

Defect No. 3 (see Table 2) which is a vertical loose zone made of crushed rock was detected by the vertical high resistivity area (Fig. 13a–c).

The areas with high resistivity close to Defect No. 4 (see Table 2), which is a concrete cube, are not clearly pointing to the location of this defect. In Fig. 13a–c, black bounding boxes at the centre of the areas with high resistivity are placed. The resistivity of the concrete is however not known, and the contrast relative to the core material might be relatively small.

In the synthetic inversion models, some high resistivity areas around Defect No. 2, 3 and 4 which were modelled as cubes or cuboids with high resistivity were observed which is partly the same for the inversion model with the field data (Figs. 12b, c, 13a–c). In the synthetic models, there is a shift location between Defect No. 4 and the high-resistivity area and, similarly, a shift location also exists in the inversion model of filed data for Defect No. 4.

Defect No. 5 (see Table 2), which is a horizontal permeable zone made of crushed rock, was not detected at all; however, it was detected by the synthetic inversion models (Figs. 12b, c, 13a–c). Reasons that contribute to this can be related to the small size and low resistivity contrast with the surrounding core material. Additionally, the defect did not lead to a sufficient flow of water that is associated with a seasonal variation in resistivity that would help ERT to detect it, for the same reasons as Defect No. 2.

Other areas than the simulated defects with high resistivity values (the yellow bounding boxes in Fig. 13a–c) were discovered which could be related to other installations, unintentional variation in material properties, temperature or water content, that might be associated with preferential flow paths. Another possible partial explanation could be inversion artefacts, but the synthetic modelling results suggest that this is not the case.

Figure 14 presents the inversion results of field data in the core from the time frame 2022-01-28, corresponding to when the water level was close to the maximum level. The results in the core are taken out without the rest of the model as it is of main interest (see the uncovered core in Fig. 11).

Its structure is similar to the results of average, maximum and minimum inverted resistivity values, and Defect No. 2 and 4 with some distance from the real location were discovered. Defect No. 3 was also detected by a vertical area with high resistivity, which can also be identified as a circular high resistive feature in the upper part of the core, marked by a green arrow in Fig. 14. Additionally, similar to the results of average, maximum and minimum inverted resistivity values, defects No. 1 and 5 were not discovered and ERT could detect some areas with high resistivity other than the simulated defects which are shown by yellow bounding boxes (Fig. 14).

The inverted resistivity values of 11 cells located along the symmetry line of the core (Fig. 15) are plotted versus time (from 2019-12-12 to 2022-01-28) in Fig. 16a. Cells No. 1–5 are located in the middle of Defects No. 1–5. Cells No. 6–9 are in the middle of the areas detected with high resistivity by the inversion models (the yellow bounding boxes in Fig. 13a). Additionally, Cells No. 10 and 11 were selected in areas which are supposedly located in areas with healthy material and not showing high inverted resistivity values in the inversion models also (Fig. 15).
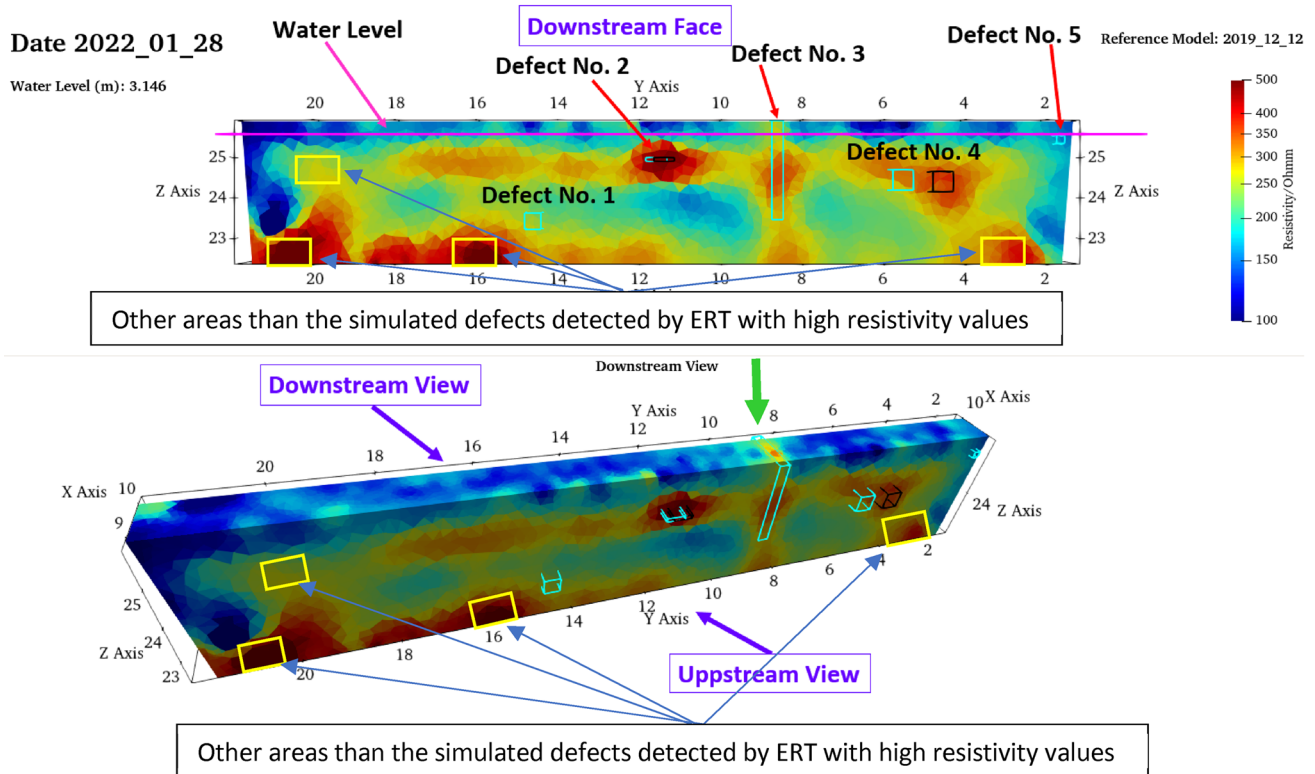
Fig. 14 The inverted field ERT data of the time frame 2022–01-07; the location of the defects is shown by blue cuboids, whereas the predicted location is indicated by black cuboids (color figure online)
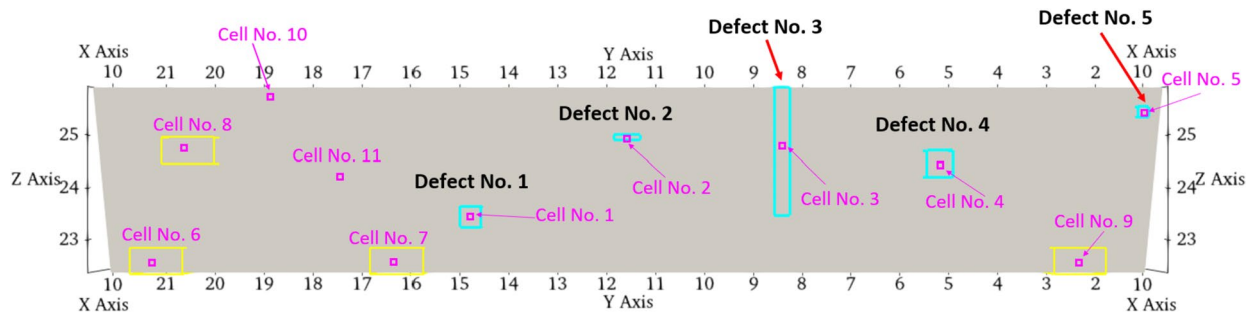
Fig. 15 The location of the cells chosen for plotting their resistivity versus time

The cells with a similar resistivity pattern in time are plotted in the same graph which leads to having four graphs each containing the resistivity versus time of Cells No. 5 and 10, Cells No. 1 and 11, Cells No. 2, 3, 4, 7 and 8, and Cells No. 6 and 9 (Fig. 16a). The reservoir water level is also plotted versus time (from 2019-12-12 to 2022-01-28) in Fig. 16b. The water temperature and temperature of Cell No. 11 are also plotted versus time (from 2019-12-12 to 2022-01-28) in Fig. 16c. A temperature sensor in fibre-optic cables is located near Cell No. 11 which made it possible to have the temperature in the vicinity of Cell No. 11 (Fig. 16c).

The resistivity values for all of the cells between 2020-07-01 and 2022-02-01 follow a pattern that shows that as the temperature decreases (see Fig. 16a, c), the resistivity increases and then as the temperature starts increasing (around 2021-03-01) the resistivity starts decreasing simultaneously (see Fig. 16a, c). It should be noted that the temperature changes affected Cells No. 2 and 6 more, which were discovered as significantly high-resistivity areas in the resistivity models (see Fig. 13a–c). It might be related to having more seeped water through these areas that can pass on the temperature variations faster.

All of the cells except for Cell No. 6 showed stable resistivity values before the dam impoundment on 2020-03-17. As the intake of water starts, the resistivity fluctuations start concurrently (Fig. 16a). This can be because as water flows, it can transfer the temperature changes inside the dam body and these temperature changes affect the resistivity values. Furthermore, as water flows it can carry fine material, depositing them and causing the resistivity variations of the material.

As mentioned before, Cells No. 2 and 6 showed faster resistivity reaction to the temperature decrease that started around 2020-07-01 (Fig. 16a). Defect No. 2, which has Cell No. 2 in the middle, was discovered by ERT data with a good resolution and very high resistivity values in comparison to the surrounding core material (see Fig. 13a–c). Cell No. 6 was also detected with a high-resistivity area (see Fig. 13a–c). It might be related to the permeable material around Cells No. 2 and 6, through which the water flows quickly, transferring temperature variations and washing out finer materials.

In Fig. 16c, the temperature of Cell No. 11 is plotted. It shows that the temperature of the cell before the dam impoundment on 2020-03-17 is stable and then starts fluctuating with the same pattern as the water temperature. After about 2021-08-01, there is a lag between the water temperature and the temperature of the cell. This suggests that over time, the dam material begins to heal, slowing down the water flow and reducing the transfer of temperature variations within the dam. It takes longer for the water to permeate the dam body, as the initial water paths become sealed and closed (Fig. 16c).

Cells No. 5 and 10 which are located near the top of the core show lower resistivity values than the other cells (between 60 and 200 Ωm) and have a similar resistivity pattern to each other (Fig. 16a). The reason that Defect No. 5 which has Cell No. 5 in the middle could not be detected by ERT (see Fig. 13a–c) can be related to having the same behaviour as the areas with healthy core material, since Cell No. 10 is located on the top of the core and in the area which is supposed to be composed of the healthy core material (Fig. 16a).

Cells No. 1 and 11 show a very similar resistivity pattern and have resistivity values between 100 and 300 Ωm. Defect No. 1, in which Cell No. 1 is located in the centre, could not be detected by ERT (see Fig. 13a–c). Since the resistivity values of Cell No. 1 are relatively similar to those of Cell No. 11, which has normal resistivity values, it demonstrates that Defect No. 1 had similar behaviour to the other core material. Since it does not have any significant resistivity contrast with the core material, it cannot be detected by ERT.

Cells No. 2, 3, 4, 7 and 8 follow a similar resistivity pattern during the whole period (Fig. 16a). All of these areas show higher resistivity values in the ERT models (Fig. 13a–c). Cells No. 6 and 9, which are both located near the bottom left and right corners, respectively, have a similar resistivity pattern and show high resistivity values in the inversion models as well (Figs. 13a–c, 16a).

For Cells No. 1, 6, 7, 9 and 11, there is a rapid resistivity increase around 2020–04-01, which is slight after the dam impoundment and a gradual resistivity decrease 3 months later (Fig. 16a). It might be related to the quick washing out of fine material happening with the dam impoundment and healing a few months after. Fine core materials are usually electrically conductive in comparison to filter or structural fill materials.
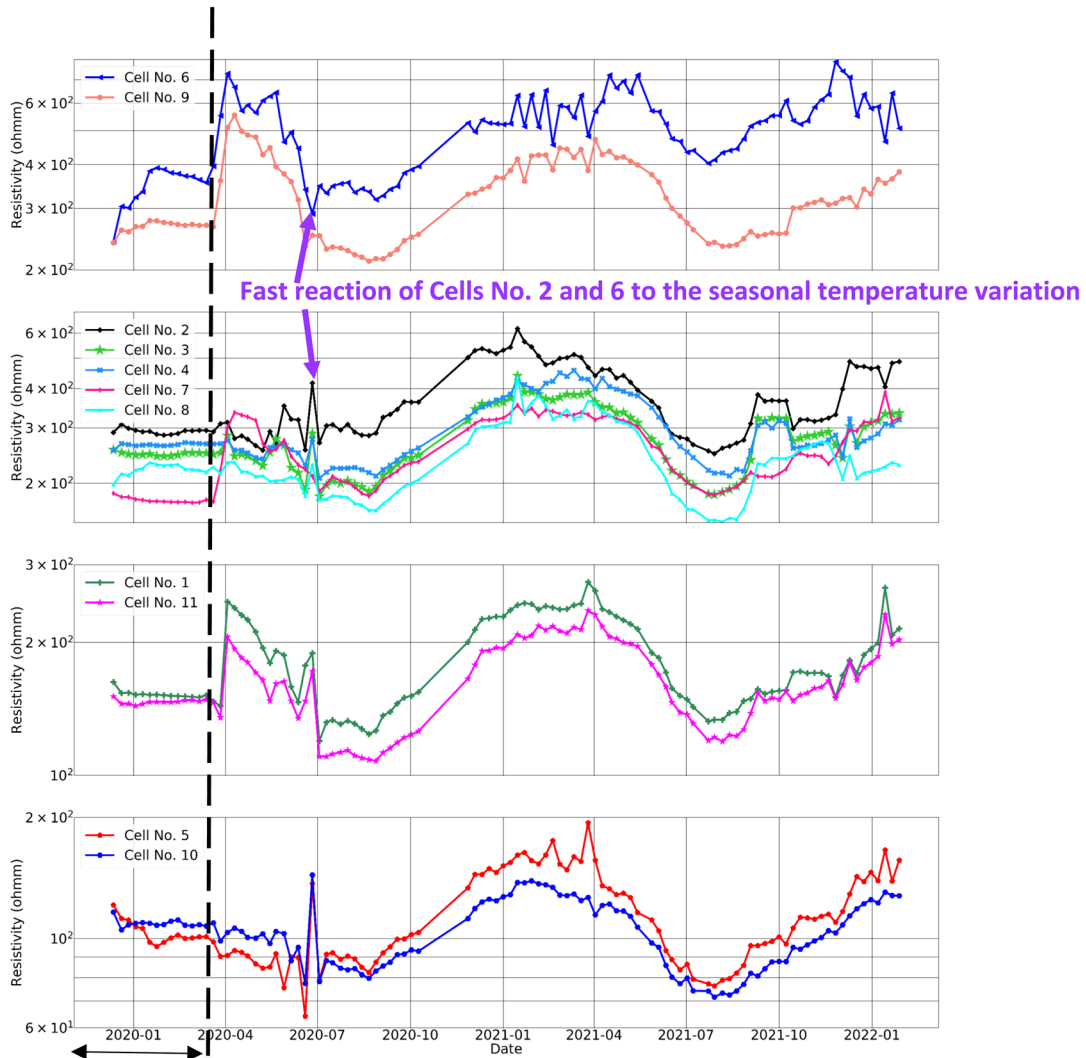
ERT was successful in discovering the defects which were a permeable horizontal zone through the core (Defect No. 2), a vertical loose zone (Defect No. 3) and a concrete block in the core (Defect No. 4). These were associated with higher resistivity, and as zones affected by internal erosion are expected to have higher resistivity values in comparison to the surrounding intact core material in typical Swedish dams, this indicates potential for detecting such.

The wooden block in the core (Defect No. 1), which was intended to simulate a cavity, was not detected. The failure to detect, apart from its size, could be related to insufficient resistivity contrast with the surrounding core material, since water-saturated wood can have a resistivity value of less than 100 Ωm.

Additionally, the defect near the abutment (Defect No. 5) was not indicated by the results. This could be related to it being small and having low resistivity contrast with the surrounding healthy core material. On the other hand, a permeable defect that goes through the core would be associated with the anomalous flow and coupled seasonal temperature-induced resistivity variation and therewith associated seasonal variation in resistivity. Due to the limited anomalous throughflow, time-lapse evaluation of the ERT data is in this case of limited value compared to data analysis for detecting a similar zone with internal erosion for a real dam [27].

The results of inversion models in the core showed that time-lapse ERT data was not able to predict the size of the defects, but capable of giving hints about the approximate locations of the defects which is valuable. It should be acknowledged that some defects are very small relative to the detection capability of ERT, and for larger defects, it is anticipated that it could give some information about the relative shapes of defects as well.

One defect was also placed inside the upstream fine filter (Defect No. 6, see Table 2). This defect was not detected by any of the inversion models, which was expected due to limited contrast in resistivity in combination with low coverage outside the core.
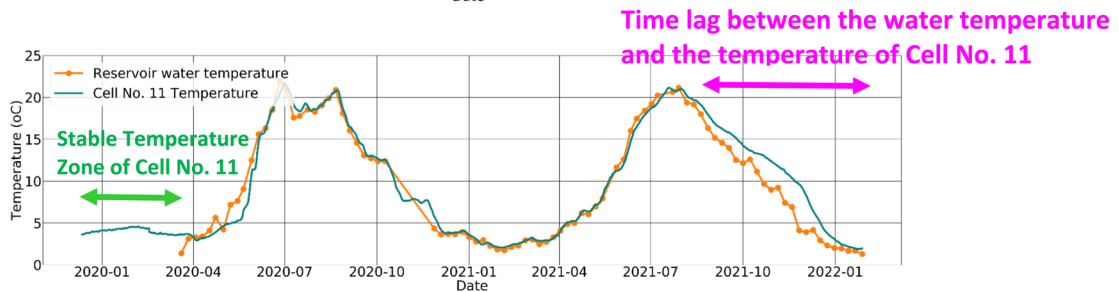
a
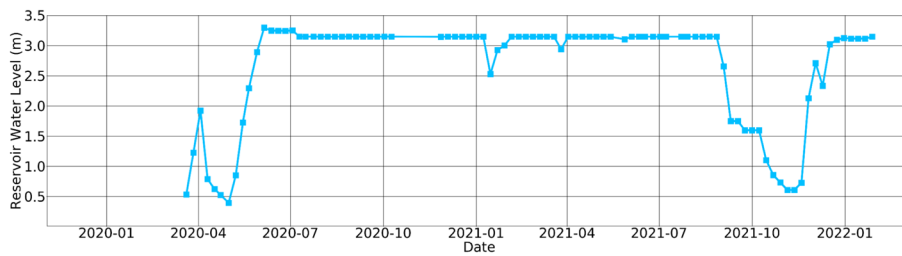
b

c

◄**Fig. 16 a** The inverted resistivity values of the selected cells versus time (from 2019-12-12 to 2022-01-28). **b** Reservoir water level versus time (from 2019-12-12 to 2022–01-28). **c** Reservoir water temperature and temperature of Cell No. 11 versus time (from 2019-12-12 to 2022-01-28)

4 Conclusions

A novel 3D approach for electrical resistivity tomography (ERT) was used to assess the capability of ERT in locating internal defects inside a test embankment dam, where some of the defects were intended to simulate internal erosion. The test embankment dam contained five defects inside the core and one in the fine filter, and the ERT measurements were conducted daily. The electrode installations and measurement sequences were designed to provide good sensitivity coverage of the core to optimize the detection capability for the defects.

Reciprocal error analysis shows that the data quality is mostly very good, with less than 1% error. The crest electrode layouts showed slightly higher errors, varying with time and reaching up to some percent, but there is no obvious explanation for this.

A 3D model inversion approach with 3D computations of the geometric factor was used for the interpretation of the data. In one of the inversion rounds, weekly data sets from the period when the water level in the reservoir was fluctuating were used. In two others, only the data sets when the water level in the reservoir was constant or decreasing were used. In all inversions, the maximum, minimum and average inverted resistivity values were calculated to have a better overall view of the time-lapse inversion models. Since the inversion models in this case contain large numbers of data and time frames, it is difficult to interpret the results and statistical parameters can simplify the interpretation of the results.

Summing up the results of all inversion models, ERT revealed a strong layering in the resistivity of the core, which is most likely caused by differential wetting of the core as suggested by geotechnical sensors. The results also discovered several anomalous zones that are not associated with the intentional defects, which could be related to buried sensors and cables for other methods, other installations or unintentional variations in material properties, temperature or water content, which could be associated with preferential flow paths and differential wetting. Such variation in resistivity might contain valuable information that is related to the long-term performance of the dam.

ERT was successful in discovering the centrally placed horizontal permeable zone and the vertical loose zone. These defects mimic zones affected by internal erosion that are

expected to have higher resistivity values in comparison to the surrounding healthy core material in typical Swedish dams, and the results thus indicate the potential for detecting internal erosion.

One defect in the form of a concrete block was vaguely indicated, and two of the defects in the core were not detected. The time series analyses showed that the two undetected core defects had similar resistivity behaviour to the surrounding healthy core material. This leads to insufficient resistivity contrast with the surrounding material and not being detectable by ERT. The small size in combination with limited or no anomalous throughflow would also cause ERT to not be able to detect some of the defects. The defect that was placed inside the fine filter was not detected, which can be attributed to limited contrast in resistivity in combination with low coverage outside the core.

The tests presented here cannot be used to fully evaluate the capability of ERT monitoring to detect internal erosion under typical Swedish conditions for more than one reason. The permeable defects that go through the core have very limited seepage of water that would be associated with a seasonal variation in resistivity, which is expected to be a key mechanism for defect detection in practical application. This was intentional and achieved by the design of the defects in combination with their shallow locations. Furthermore, for larger dams, scale effects and practical limitations for electrode installations need to be taken into account and evaluated as well.

Declarations

References

1. Binley A, Slater L (2020) Resistivity and induced polarization—theory and applications to the near-surface earth. Cambridge University Press, p 388. ISBN: 978-1-108-49274-4.

2. Sjödahl P, Dahlin T, Johansson S, Loke MH (2008) Resistivity monitoring for leakage and internal erosion detection at Hällby embankment dam. J Appl Geophys 65:155–164

3. Dahlin T, Sjödahl P, Friborg J, Johansson S (2001) Resistivity and SP Surveying and Monitoring at the Sädva Embankment Dam, Sweden. In: Mistømme GH, Honningsvåg B, Repp K, Vaskinn KA, Westeren T (eds) Dams in a European context, Balkema, Lisse, pp 107–113. ISBN: 90 5809 196 1

4. Sjödahl P, Dahlin T, Johansson S (2010) Using the electrical resistivity method for leakage detection in a blind test at the Røssvatn embankment dam test facility in Norway. Bull Eng Geol Environ 69:643–658

5. Sjödahl P, Johansson S, Dahlin T (2011) Investigation of shallow leakage zones in a small embankment dam using repeated resistivity measurements in Internal erosion in embankment dams and their foundations. Fry J-J, Riha J, Julinek T (eds), pp 165–172. ISBN: 978-80-7204-736-9

6. Martínez-Moreno FJ, Delgado-Ramos F, Galindo-Zaldivar J, Martín-Rosales W, López-Chicano M, González-Castillo L (2018) Identification of leakage and potential areas for internal erosion combining ERT and IP techniques at the Negratín Dam left abutment (Granada, southern Spain). Eng Geol 240:74–80

7. Masi M, Ferdos F, Losito G, Solari L (2020) J Hydrol 589:125340

8. Shin S, Park S, Kim JH (2019) J Appl Geophys 170:103834

9. Lee B, Oh S, Yi MJ (2020) Mapping of leakage paths in damaged embankment using modified resistivity array method. Eng Geol 266:5

10. Hojat A, Ferrario M, Arosio D, Brunero M, Ivanov VI, Longoni L, Madaschi A, Papini M, Tresoldi G, Zanzi L (2021) Laboratory studies using electrical resistivity tomography and fiber optic techniques to detect seepage zones in river embankments. Geosciences 11:69

11. Y Guo C Yian J Xie Y Luo P Zhang H Liu J Liu 2022 Seepage detection in earth-filled dam from self-potential and electrical resistivity tomography Eng Geol 306 106750

12. Cho IK, Ha IS, Kim KS, Ahn HY, Lee S, Kang HJ (2014) 3D effects on 2D resistivity monitoring in earth-fill dams. Near Surf Geophys 12:73–81

13. Fargier Y, Palma Lopes S, Fauchard C, Francois D, Cote P (2014) DC-Electrical resistivity imaging for embankment dike investigation: a 3D extended normalisation approach. J Appl Geophys 103:245–256

14. Bièvre G, Oxarango L, Günther T, Goutaland D, Massardi M (2018) Improvement of 2D ERT measurements conducted along a small earth-filled dyke using 3D topographic data and 3D computation of geometric factors. J Appl Geophys 153:100–112

15. Norooz R, Olsson PI, Dahlin T, Günther T, Bernstone C (2021) J Appl Geophys 191:104355

16. Bernstone C, Lagerlund J, Toromanovic J, Juhlin C (2021) Deformationer och portryck i en experimentell fyllningsdamm. Energiforsk report.

17. Lagerlund J, Bernstone C, Viklander P, Nordström E (2022) Embankment test dam of Älvkarleby—description of installed defects and their position. Mendeley Data. V3

18. Rücker C, Günther T (2011) The simulation of finite ERT electrodes using the complete electrode model. Geophysics 76(4):F227-238. https://doi.org/10.1190/1.3581356

19. Zhou B, Greenhalg SA (2000) Cross-hole resistivity tomography using different electrode configurations. Geophys Prospect 48:887–912

20. Zhou B, Bouzidi Y, Ullah S, Asim M (2020) A full-range gradient survey for 2D electrical resistivity tomography. Near Surf Geophys 18(6):609–626

21. Dahlin T, Zhou B (2006) Gradient array measurements for multichannel 2D resistivity imaging. Near Surf Geophys 4(2):113–123

22. Tejero-Andrade A, Cifuentes G, Chávez RE, López-González AE, Delgado-Solórzano C (2015) L- and CORNER-arrays for 3D electric resistivity tomography: an alternative for geophysical surveys in urban zones. Near Surf Geophys 13:355–367

23. Ingeman-Nielsen T, Tomaškovičová S, Dahlin T (2016) Effect of electrode shape on grounding resistances—part 1: the focus-one protocol. Geophysics 81(1):WA159–WA167

24. Udphuay S, Günther T, Everett ME, WardenBriaud RJL (2011) Three-dimensional resistivity tomography in extreme coastal terrain amidst dense cultural signals: application to cliff stability assessment at the historic D-Day site. Geophys J Int 185(1):201–220. https://doi.org/10.1111/j.1365-246X.2010.04915.x

25. Loke MH (2011) Electrical resistivity surveys and data interpretation. In: Gupta H (ed) Solid earth geophysics encyclopedia. "Electrical & electromagnetic," 2nd edn. Springer Verlag, pp 276–283

26. Günther T, Rücker C, Spitzer K (2006) 3-D modeling and inversion of DC resistivity data incorporating topography—part II: inversion. Geophys J Int 166:506–517. https://doi.org/10.1111/j.1365-246X.2006.03011.x

27. Rücker C, Günther T, Wagner FM (2017) pyGIMLi: an open-source library for modelling and inversion in geophysics. Comput Geosci 109:106–123

28. Si H (2015) ACM Trans Math Softw (TOMS) 41:36

29. Sjödahl P, Dahlin T, Zhou B (2006) 2.5D resistivity modeling of embankment dams to assess influence from geometry and material properties. Geophysics 71:107–114

30. Schön J (1996) Physical properties of rocks: fundamentals and principles of petrophysics. Handbook of geophysical exploration, vol 18. Redwood Books, Trowbridge

31. Schopper JR (1982) Electrical conductivity of rocks containing electrolytes Landolt-Börnstein, Group V, vol 16, Physical properties of rocks. Springer, pp 276–291

32. Fediuk A, Wilken D, Wunderlich T, Rabbel W (2020) Physical parameters and contrasts of wooden objects in lacustrine environment: ground penetrating radar and geoelectrics. Geosciences 10:146